Vol. 15, No. 2 (2026): 510 - 524 https://dx.doi.org/10.23960/jtepl.v15i2.510-524

JURNAL TEKNIK PERTANIAN LAMPUNG

ISSN 2302-559X (print) / 2549-0818 (online)
Journal homepage : https://jurnal.fp.unila.ac.id/index.php/JTP

Ray Tracing-Based Modeling of Bifacial Photovoltaic Systems in Greenhouse Agrivoltaics

Endang Widiyawati[1], Subiyanto[1,✉], Budi Sunarko[1], Siti Ridloah[1], Bagaskoro Saputro[2], Rizky Ajie Aprilianto[1], Mario Norman Syah[1], Abdurrakhman Hamid Al-Azhari[1], Deyndrawan Sutrisno[1], Aisya Fathimah[1], Apriansyah Wibowo[1], I Gede Bagus Jayendra[1]

[1] Department of Electrical Engineering, Faculty of Engineering, Universitas Negeri Semarang, INDONESIA.

[2] BINUS University, Semarang, INDONESIA

Article History:

Received : 16 July 2025
Revised : 08 October 2025
Accepted : 16 October 2025

Keywords:

Bifacial photovoltaic,
Greenhouses,
Photosynthetically active radiation,
Ray tracing.

Corresponding Author:
✉ subiyanto@mail.unnes.ac.id
(Subiyanto)

ABSTRACT

This work presents an enhanced ray tracing-based modeling framework to optimize bifacial photovoltaic energy generation and crop productivity within greenhouse environments. The proposed framework integrates a ray tracing-based optical and electrical model to simulate light dynamics and energy generation within greenhouse structures. The optical model incorporates Uniform Distribution of rear-irradiance (UF) and Non-Uniform Distribution of rear-irradiance (NUF) principles to simulate irradiance distribution, shading, and reflection, using Light Saturation Point (LSP) and Photosynthetically Active Radiation (PAR) measurements. The electrical model estimates energy yield using the LambertW function based on incident and transmitted light through photovoltaic arrays. Five types of greenhouse structures using plastic and SG80 materials are analyzed to assess their impact on system performance under various conditions. The evaluation showed that integrating bPV increased rear-side energy captured by 25-30%. The optimal configuration was achieved by combining a plastic cover with a checkerboard pattern, resulting in up to 5% higher performance than the 35° tilt setup and offering enhanced light distribution uniformity. Although the average soil irradiance of 170.801 W/m² slightly exceeded the light saturation threshold of 164.7 W/m², it remained within a safe range that supports efficient photosynthesis without causing photoinhibition.

1. INTRODUCTION

The growing demand for residential and industrial development has challenged agricultural land use, leading to the adoption of agrivoltaic systems that combine solar energy production with farming to optimize land use and maintain productivity (Mamun *et al*., 2022). To further enhance the performance of such systems, Bifacial Photovoltaic (bPV) systems, which capture sunlight on both the front and rear sides of the panels, have become a focal point in optimizing solar energy generation, particularly when integrated into agrivoltaic systems (Teitel *et al*., 2023; Zhang *et al*., 2024). These systems, designed to combine food production with clean energy generation, are gaining traction as a sustainable approach to meet the increasing demand for both energy and food (Katsikogiannis *et al*., 2022). However, optimizing the energy output from bifacial PV systems while ensuring favorable crop growing conditions requires a deep understanding of light interactions within the greenhouse environment (Angmo *et al*., 2022). This entails evaluating how light is distributed across the greenhouse, including its effects on both PV modules and plant growth (Leng *et al*., 2023).

Recent studies have highlighted the potential of bifacial PV systems to significantly increase energy production by utilizing reflected light, especially in environments with high albedo or under overcast conditions (Ernst *et al*., 2024a; Zhang *et al*., 2025b). Researchers have developed various strategies, such as optimizing panel configurations (e.g., tilted or checkerboard patterns), to enhance light distribution and reduce shading, thus supporting crop growth while maximizing solar energy output (Ayala Pelaez, 2019; Ernst *et al*., 2024b; Laue, 2022). Despite these advancements, computational challenges remain, particularly concerning the precision and efficiency of simulations used to model light distribution in these systems (Lewis *et al*., 2024; Robsahm, 2023).

Ray Tracing has proven effective for accurately modeling light interactions in bifacial PV systems (Ernst *et al*., 2022), yet large-scale simulations still demand substantial computational resources (Grommes *et al*., 2023; Zhang *et al*., 2025a). Moreover, many existing models overlook environmental factors such as temperature and humidity, which strongly influence both PV performance and crop development (Russell *et al*., 2022). In agrivoltaic applications, ray tracing plays a key role by linking solar energy modeling with crop light availability, thus supporting dual optimization of energy yield and agricultural productivity (Laue, 2022). To overcome current limitations, an integrated modeling approach that combines geometric, environmental, and material parameters is essential for improving predictive accuracy and practical applicability (Hansen *et al*., 2016; Kujawa *et al*., 2025).

This work presents an enhanced ray tracing-based modeling framework for bPV systems in greenhouse settings to simultaneously improve energy generation and crop growth. Using Bifacial Radiance, the model simulates irradiance distribution and estimates energy yield through regression analysis. It also integrates Light Saturation Point (LSP) and Photosynthetically Active Radiation (PAR) measurements to assess crop light availability. Overall, the framework provides a reliable basis for optimizing agrivoltaic design toward higher efficiency and sustainable land use.

2. MATERIALS AND METHODS

The proposed bifacial agrivoltaic framework, as shown in Figure 1, begins with the characterization of bifacial PV modules to determine the bifacial gain coefficient (φ) from short-circuit current measurements. This coefficient informs a coupled optical-electrical model, where 3D ray tracing produces rear-irradiance non-uniform (NUF), later refined through regression. NUF and φ are used to estimate surface irradiance, capacity factor, and dynamic bifacial energy yield, while the optical model independently evaluates PAR reduction to optimize both energy production and crop lighting.

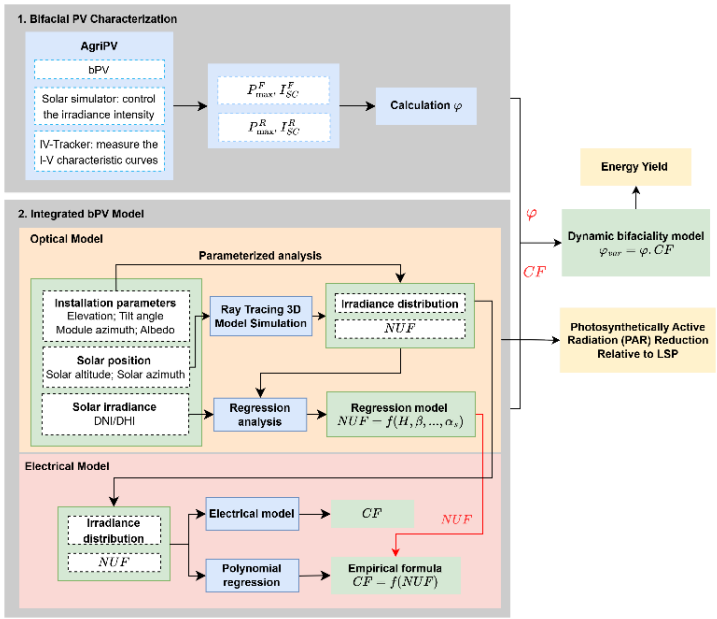

Figure 1. Proposed framework for bifacial agrivoltaic

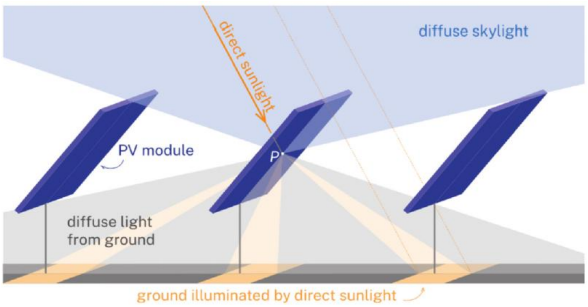

Figure 2. The illumination states and modeling of bifacial photovoltaic

2.1. Bifacial Photovoltaic Formulation

The bifacial photovoltaic system in Figure 2 captures front and rear irradiance from sunlight, sky, and ground albedo to boost energy output, while tilt optimization and sensor monitoring assess light effects on shade-tolerant crops below (Ernst *et al*., 2024a). Bifaciality, defined as the minimum ratio of rear to front surface performance G_F, is quantified as static bifaciality φ_{stc} using Equation (1) in IEC (2022), with factor φ calculated from short-circuit current ($I^R_{sc,stc}$, $I^F_{sc,stc}$) and power output ratios ($P^R_{max,stc}$, $P^F_{max,stc}$), normalized by irradiances G_F and G_R using Equation (2), while dynamic bifaciality (φ_{var}) in Equation (3) accounts for irradiance variations and non-uniform rear distribution.

$$\varphi_{stc} = \min\left(\frac{I^R_{sc,stc}/G_R}{I^F_{sc,stc}/G_F}, \frac{P^R_{max,stc}/G_R}{P^F_{max,stc}/G_F}\right) = min\left(\frac{I^R_{sc,stc}}{I^F_{sc,stc}}, \frac{P^R_{max,stc}}{P^F_{max,stc}}\right) \quad (1)$$

$$\varphi = \min\frac{I^R_{sc}/G_R}{I^F_{sc}/G_F}, \frac{P^R_{max}/G_R}{P^F_{max}/G_F} \quad (2)$$

$$\varphi_{var} = \varphi CF \quad (3)$$

The correction factor for bifaciality, abbreviated as *CF*, measures how variations in irradiance across the rear surface affect the module's overall bifacial response. These variations, described by the non-uniform (NUF), represent differences in the amount of light received at different rear-side areas of the photovoltaic module. The value of NUF is derived following the formulation provided in Equation (4) as presented in Hansen *et al*. (2016); International Electrotechnical Commission (2022).

$$NUF = \frac{G^R_{max} - G^R_{min}}{G^R_{max} + G^R_{min}}.100\% \quad (4)$$

The maximum and minimum irradiance intensities on the rear side of the bifacial photovoltaic module are represented by G^R_{max} and G^R_{min} respectively. Based on these values, the bifaciality correction factor *CF*, which accounts for the effects of rear irradiance non-uniformity, is determined using Equations (5) through (7).

$$CF = \frac{\varphi_{nuf}}{\varphi_{uf}} \quad (5)$$

$$\varphi_{nuf} = \min\left(\frac{I^R_{sc,nuf}}{I^F_{sc,uf}}, \frac{P^R_{max,nuf}}{P^F_{max,uf}}\right) \quad (6)$$

$$\varphi_{uf} = \min\left(\frac{I^R_{sc,uf}}{I^F_{sc,uf}}, \frac{P^R_{max,uf}}{P^F_{max,uf}}\right) \quad (7)$$

The parameters φ_{nuf} and φ_{uf} represent the bifaciality under conditions of nonuniform and uniform rear-side irradiance distribution, respectively. The terms $I^R_{sc,nuf}$ and $I^F_{sc,uf}$ refer to the short-circuit current generated by the rear side when exposed to nonuniform and uniform irradiance conditions. Correspondingly $P^R_{max,nuf}$ and$P^F_{max,uf}$, describe the maximum power output from the rear side under these respective conditions. Furthermore, the values $I^F_{sc,uf}$ and $P^F_{max,uf}$ represent the short-circuit current and the maximum power output of the front side when subjected to uniform irradiance.

2.2. Ray Tracing for Optical Model

A ray tracing–based model was developed to evaluate irradiance across user-defined x, y, and z coordinates, as shown in Figure 3, which illustrates ray interactions including specular and diffuse reflection from the greenhouse structure, transmission through the cover material, and absorption by PV modules (Kujawa *et al*., 2025).

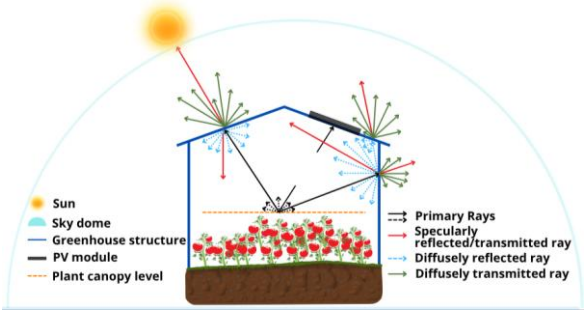

Figure 3. Schematic diagram of the ray tracing procedure for a greenhouse

The bifacial photovoltaic system was modeled using the bifacial_radiance tool (Ayala Pelaez & Deline, 2020) to evaluate light distribution in agrivoltaic settings, incorporating specular and diffuse irradiance. System geometry and optics were defined as inputs, with module surfaces modeled using a 3D ellipsoidal Equation (8) for accurate light interaction. The overall sequence of the ray tracing simulation steps is illustrated in Figure 4, which depicts the flowchart of the algorithm used to compute irradiance at each defined spatial location.

$$F(x_1, x_2, x_3) = \left|\frac{x_1 - x_{1o}}{R_1}\right|^{p1} + \left|\frac{x_2 - x_{2o}}{R_2}\right|^{p2} + \left|\frac{x_3 - x_{3o}}{R_3}\right|^{p3} \quad (8)$$

Parameters R_1, R_2, R_3 denote the ellipsoid radii p_1, p_2, p_3 defining curvature in each axis, and x_{1o}, x_{2o}, x_{3o} represent the center coordinates. Parameters. A ray intersects a panel if $f(x_{1,j}, x_{2,j}, x_{3,j}) \leq 1$ and ground contact occurs when $x_{3,j} \leq 0$. To simulate solar input, incoming sunlight is discretized into individual rays, each assigned an initial power. Upon intersecting a surface, the simulation determines the local surface orientation. These processes are governed by Equations (9) and (10).

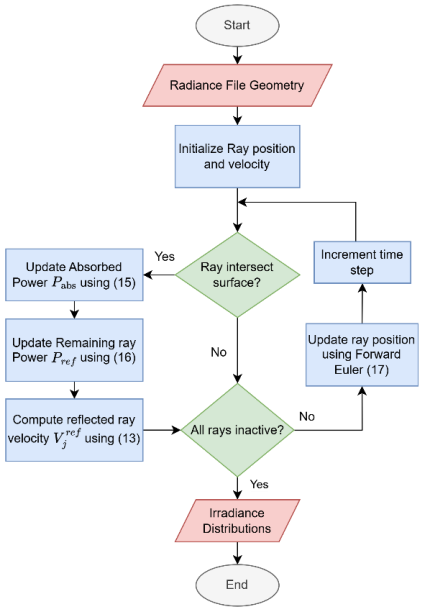

Figure 4. Flowchart ray tracing algorithm

$$P_r = \frac{P_{tot} A_b}{N_r} \tag{9}$$

$$\mathrm{n} = -\frac{\nabla F}{\|\nabla F\|} \tag{10}$$

Equation (9) defines is the initial power per ray P_r, calculated from the total irradiance P_{tot}, which is sourced from meteorological data. A_b represents the cross-sectional area of the beam, and N_r is the total number of rays used in the simulation. Equation (10) defines the inward-pointing surface normal n, obtained from the normalized gradient of the implicit surface function F. For a flat surface such as the ground, this simplifies to $\mathrm{n} = [0,0,-1]$. After identifying surface contact, the simulation models the rays' optical interaction calculating the incidence angle, decomposing the velocity vector, determining the reflected direction, and evaluating reflectance. These steps were described by Equations (11) to (14).

$$\theta_i = cos^{-1}\left(\frac{v_j . \mathrm{n}_j}{\|v_j\| \|\mathrm{n}_j\|}\right) \tag{11}$$

$$v_{j,\perp} = \|v_j\| cos\theta_i \mathrm{n}_j \tag{12}$$

$$v_j^{ref} = v_j - 2v_{j,\perp} \tag{13}$$

$$l\mathcal{R}(\hat{n}, \theta_i) = \frac{I_r}{I_i} \tag{14}$$

Equation (11) calculates the angle of incidence θ_i based on the dot product between the ray velocity v_j and the surface normal n_j Equation (12) expresses the perpendicular component of the ray's velocity $v_{j,\perp}$, projected onto the surface normal. Equation (13) determines the direction of the reflected ray v_j^{ref} by subtracting twice the perpendicular component from the original velocity. Equation (14) defines the reflectance $l\mathcal{R}$ as the ratio of reflected to incident energy, influenced by the angle θ_i and the refractive index ratio $\hat{n}$, following the Fresnel model as outlined in (Zohdi, 2021). The process begins with geometry initialization and ray setup, followed by surface intersection checks. When a ray hits a surface, absorbed and remaining power are updated using Equations (15) and (16). Ray positions are then advanced via the Forward Euler method in Equation (17). The loop continues until all rays become inactive, producing the final irradiance distribution.

$$P_{abs} = (1 - l\mathcal{R}) P_r \tag{15}$$

$$P_{ref} = l\mathcal{R} P_r \tag{16}$$

$$r_j(t + \Delta t) = r_j(t) + \Delta t v_j(t) \tag{17}$$

The time step Δt is defined as $\Delta \mathrm{t} = \xi \frac{h_0^{ray}}{c}$, to align temporal resolution with light propagation, where $\xi \in (0,1)$ is a scaling parameter. At each step, front and rear irradiance $E_{front}(t), E_{rear}(t)$ contributions are accumulated to compute monthly insolation, with averages calculated in Equation (18). These values serve as inputs to the energy yield model using ray-traced front and rear irradiance weighted by CF or φ.

$$Ins_{front} \approx \frac{\Delta t}{1000} \sum_{k=1}^{N} E_{front}(t_k); \quad Ins_{rear} \approx \frac{\Delta t}{1000} \sum_{k=1}^{N} E_{rear}(t_k) \tag{18}$$

To interpret the simulated irradiance results in an agronomic context, the LSP and LCP of tomato crops were considered as benchmarks. Based on prior studies, the tomato's LSP and LCP correspond to 164.7 W/m² and 8.53 W/m², respectively, after converting from PAR using a factor of 4.56 µmol J^{-1} (Teitel *et al.*, 2023). Simulated irradiance was evaluated against crop-specific thresholds to determine whether greenhouse conditions support optimal photosynthesis or pose light limitation or saturation risks.

2.3. Electrical Model

The electrical performance of bifacial photovoltaic modules is assessed by correlating spectral input with power output using circuit-based models. Models for both uniform and non-uniform conditions are applied to evaluate the impact of rear-side irradiance non-uniform. In the uniform case, an equivalent circuit model estimates power output based on the single-diode voltage-current relationship in Equation (19) (De Soto *et al*., 2006; Gu *et al*., 2020) as shown in Figure 5.

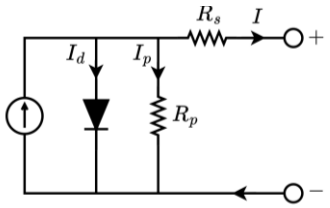

Figure 5. Equivalent circuit for a PV module

$$I = I_{ph} - I_d - I_p; \qquad I = I_{ph} - I_0\left\{exp\left(\frac{V+IR_s}{V_t}\right) - 1\right\} - \frac{V+IR_s}{R_p} \tag{19}$$

This expression describes the output current I as a function of the photogenerated current I_{ph} reduced by diode and resistive losses. The series resistance R_s and thermal voltage V_t influence both the exponential and linear components, characterizing the inherent non-linear response of the photovoltaic device.

The parameters embedded in Equation (19), I_{ph}, I_0, R_s, R_p, and V_t are determined under Standard Test Conditions (STC). These values, denoted as $I_{ph,stc}, I_{0,stc}, R_{s,stc}, R_{p,stc}$, and $V_{t,stc}$ are calculated using known voltage, current, and temperature coefficients at characteristic operating points. Due to the implicit and transcendental of Equation (19), an iterative computational approach is required to resolve the output voltage and current, often incurring significant computational cost. To alleviate this, the expression is reformulated into an explicit form through the use of the LambertW function formulated in Equation (20) (De Soto *et al*., 2006; Fathabadi, 2015; Tripathy *et al*., 2017).

$$\begin{cases} V = R_p\left(I_{ph} + I_0 - I\right) - IR_s - V_t LambertW(Y) \\ Y = \frac{I_0 R_p}{V_t} exp\left(\frac{R_p(I_{ph}+I_0-I)}{V_t}\right) \end{cases} \tag{20}$$

Under non-uniform rear irradiance, mismatch losses are assessed by evaluating five circuit parameters per cell based on localized irradiance as shown in Figure 6, with each cell's output compared to the total module output to determine its performance. Cells with lower irradiance may become reverse-bias, thereby consuming power and reducing the module's net output. The module comprises $n \times m$ cells connected in series. The parameters for each cell are calculated using Equation 21 (Xiong *et al*., 2022).

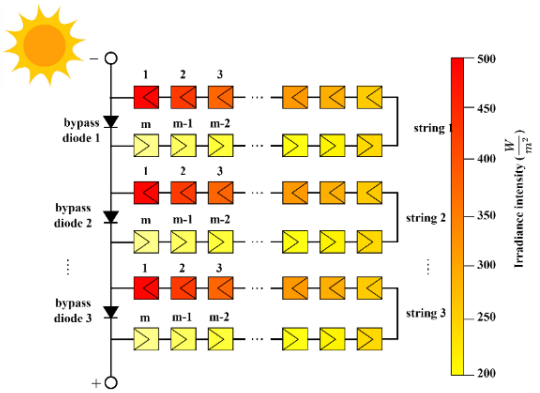

Figure 6. Schematic diagram of the internal circuit of the PV module

$$I_{ph,c} = I_{ph}; I_{0,c} = I_0; R_{p,c} = \frac{R_p}{m \times n}; \tag{21}$$

$$R_{s,c} = \frac{R_s}{m \times n}; V_{t,c} = \frac{V_t}{m \times n}$$

Where $I_{ph,c}$, $I_{0,c}$, $R_{p,c}$, $R_{s,c}$ and $V_{t,c}$ are the five parameters of the cell in the PV module. The photogenerated currents for each cell are ordered from minimum to maximum, as expressed in Equation (22).

$$I_{ph,c}^{min} = I_{ph,c}^{1} > I_{ph,c}^{2} > \cdots I_{ph,c}^{m-1} > I_{ph,c}^{m} = I_{ph,c}^{max} \tag{22}$$

The operating state of each cell is determined by comparing the module current I with the photogenerated current $I_{ph,c}^{q}$. the cell operates normally, and the voltage V_q is calculated using Equation (23). This equation incorporates cell-specific parameters $I_{ph,c}^{q}, I_{0,c}^{q}, R_{s,c}^{q}$, and $V_{t,c}^{q}$. Due to its transcendental nature, the voltage expression is reformulated into an explicit form using the LambertW function, as shown in Equation (23) - (24) (De Soto *et al*., 2006; Fathabadi, 2015; Tripathy *et al*., 2017; Zhu *et al*., 2019).

$$V_q = R_{p,c}^{q}\left(I_{p,c}^{q} + I_{0,c}^{q} - I\right) - IR_{s,c}^{q} - V_{t,c}^{q} LambertW\left(Y_c^q\right) \tag{23}$$

$$Y_c^q = \frac{I_{0,c}^{q} R_{p,c}^{q}}{V_{t,c}^{q}} \exp\left(\frac{R_{p,c}^{q}\left(I_{ph,c}^{q} + I_{0,c}^{q} - I\right)}{V_{t,c}^{q}}\right) \tag{24}$$

The intermediate term Y_c^q, defined in Equation (24), captures the nonlinear current-voltage behavior for the q^{th} in the diode model. The $I_{sc,uf}^{R}, P_{max,uf}^{R}, I_{sc,nuf}^{R}, P_{max,nuf}^{R}, I_{sc,uf}^{F}$, and $P_{max,uf}^{F}$ are calculated by the above electrical model under uniform and non-uniform irradiance distribution. Electrical parameters under uniform and non-uniform irradiance are computed and substituted into Equations (6) to (8) to derive the bifacial Correction Factor (CF), which adjusts energy yield predictions for asymmetrical irradiance. Monthly energy output E_m is calculated using Equation (25) as the product of module area A, efficiency Eff, and performance ratio PR from (Pettersen, 2019), multiplied by the sum of front and rear irradiance weighted by the bifaciality factor CF.

$$E_m = A \times Eff \times PR \times (Ins_{front} + Ins_{rear} \times CF) \tag{25}$$

2.4. Greenhouse Model

A simulation environment was conducted to assess the performance of bPV modules in a 12 × 6 × 4.5 m gable-roof structure based on local horticultural practices (Direktorat Sayuran dan Tanaman Obat, 2021). A modular approach enabled scalability without reconstructing the full model, with structural elements such as walls, roof, planting zones, and light pathways defined in 3D using the Radiance engine. Five PV configurations, varying in height, tilt, and layout Figure 7, were tested to assess light distribution, shading, and energy efficiency. Strategic sensor placements captured irradiance data at both canopy and module levels to support detailed analysis of PAR availability.

Two types of greenhouse cover materials were analyzed, and different materials were used, such as SG80 diffusive glass and white plastic. These materials were chosen for their distinct transmittance and diffusion properties, which significantly influence light penetration and the uniformity of PAR distribution. The optical and structural characteristics of the cover materials are summarized in Table 1.

Monocrystalline PERC bPV modules were simulated in a landscape orientation, accounting for both front and rear irradiance. Ground reflectivity between 0.2 and 0.3 was considered to capture rear-side gain under different surface conditions. Technical specifications of the modules are detailed in Table 2.

Table 1. Greenhouse Structural and Optical Parameters

Parameter	SG80 Diffuse Glass	White Greenhouse Plastic
Light transmittance (%)	78	70
Haze factor (%)	78	70
Thickness (mm)	3	0.2
Material type	Glass	Plastic

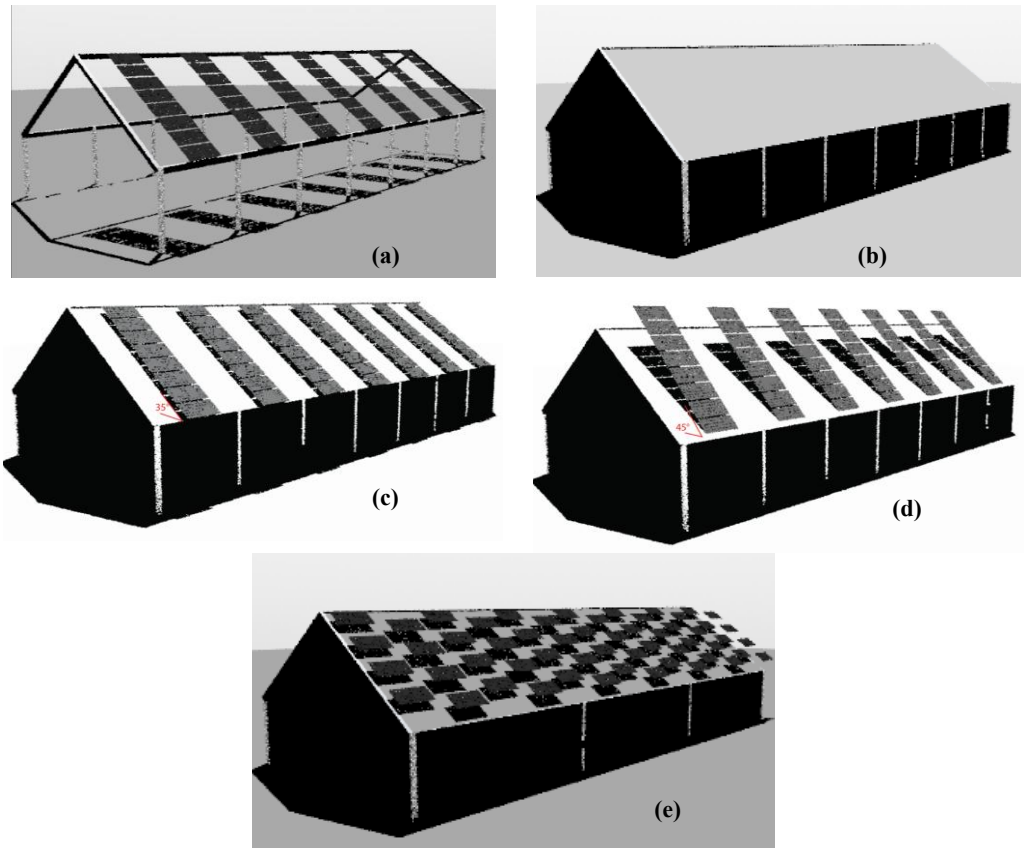

Figure 7. Greenhouse with different modules (a) structure and modules, (b) empty modules, (c) 35° tilt, (d) 45° tilt, (e) checkerboard pattern.

Table 2. PV Module Specification

Parameter	Value
Cell type	Monocrystalline PERC Bifacial
Module dimensions	2.1 m × 1.1 m
Number of cells	72 (12 × 6)
Cell size	15.6 cm × 15.6 cm
Bifaciality factor	0.7 (70%)
Module efficiency	20.38%
Module orientation	Landscape (horizontal)
Rear reflectivity	0.2 - 0.3 (based on floor properties)

3. RESULTS AND DISCUSSION

This section presents ray tracing simulation results of a bifacial agrivoltaic greenhouse, analyzing light distribution, shading, and energy output across configurations using TMY data from Semarang, Central Java (*NREL "EnergyPlus,"* 2021). The evaluation focuses on spatial and temporal variations in ground irradiance, PAR, and total energy yield to support system optimization.

3.1. Evaluation Environment Setup

A custom simulation environment is developed to evaluate the performance of bifacial agrivoltaic greenhouse systems under varying irradiance conditions. Figure 8 shows the evaluation setup with sensor arrays positioned for ground-level irradiance analysis. Two irradiance sensor arrays, Groundscan 1 and Groundscan 2, are implemented to monitor spatial light distribution. Groundscan 1 captures uniform irradiance data across the greenhouse floor, while

Groundscan 2 targets localized zones with high and low irradiance to assess shading effects. Simulations are conducted during the tomato cultivation period from mid-May to early October, recording hourly ground irradiance data. Light thresholds for photosynthesis are based on the LSP 164.7 W/m² and LCP 8.53 W/m², derived from PAR values (Bantis *et al*., 2024; Rezaei *et al*., 2024).

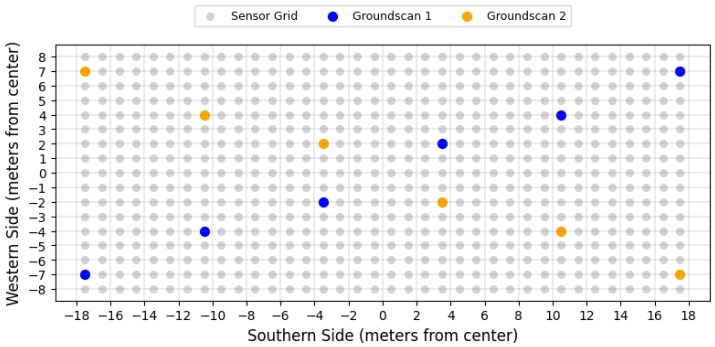

Figure 8. Evaluation environment with sensor arrangement for irradiance analysis

3.2. Ground-Level Irradiance Distribution Analysis

The results of ground-level irradiance distribution are presented in Figure 9. This evaluation shows that the structure and module-only configuration yielded the highest irradiance on all surfaces. In contrast, greenhouse-covered systems, particularly those using SG80, provided more uniform but moderated irradiance levels. Tilted and checkerboard configurations with SG80 further improved rear-side irradiance and ground-level uniformity.

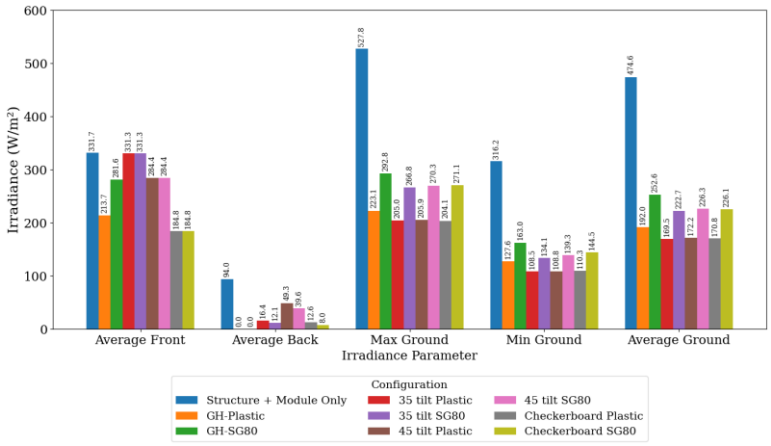

Figure 9. Comparison of ground-level irradiance across various greenhouse configurations in (W/m²)

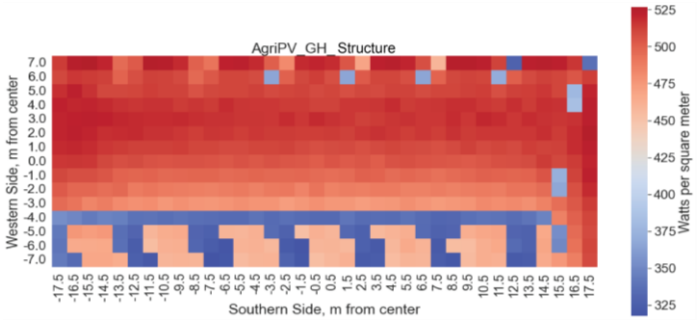

Figure 10. Heatmap of ground irradiance from the model with greenhouse structure and modules only

This model simulated the light behavior within an agrivoltaic greenhouse featuring a transparent roof without any diffusive covering, as visualized in Figure 10. Structural rails were intentionally excluded to simplify the system and to allow better assessment of shadow formation and residual irradiance. The simulated values ranged from 680 to 740 W/m², closely aligning with the satellite-based irradiance data of 757 W/m² from Solcast (2021) recorded at 11:00 a.m. on June 17, 2021, and these values were subsequently converted to photosynthetically active radiation using a conversion factor of 4.56 µmol/J (Fathabadi, 2015).

To evaluate the influence of different greenhouse coverings on light distribution, simulations were performed on greenhouse models without bPV modules. As shown in Figure 11, white plastic cover resulted in irradiance ranging from 127.65 W/m² to 223.05 W/m², while the SG80 glazing provided a more uniform distribution between 163.03 to 292.84 W/m². These results highlight the superior light diffusion of SG80 compared to conventional plastic.

To evaluate the effect of bPV tilt angle on ground-level irradiance, simulations were conducted using two roof materials at a fixed 35° tilt (Figure 12). The white plastic roof generated a peak irradiance of 205.0 W/m² and output of 152.51 W but resulted in uneven light distribution due to limited scattering. In contrast, the SG80 roof achieved a more uniform irradiance with an average of 222.71 W/m².

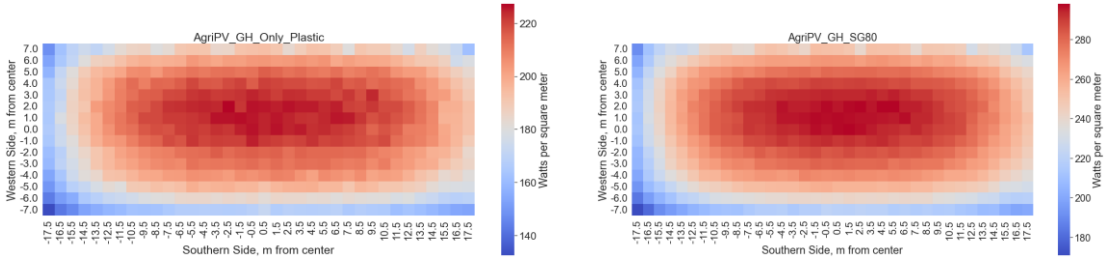

(a) (b)

Figure 11. Heatmaps of ground irradiance with diffuse covers: (a) plastic-based, (b) SG80-based

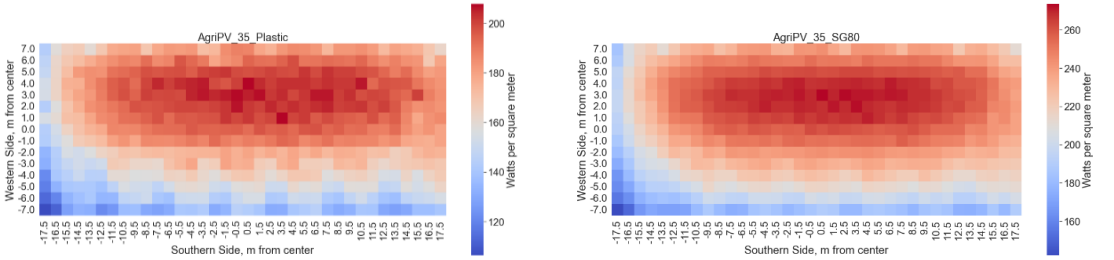

(a) (b)

Figure 12. Heatmaps of ground irradiance with modules at a 35° tilt: (a) plastic-based, (b) SG80-based

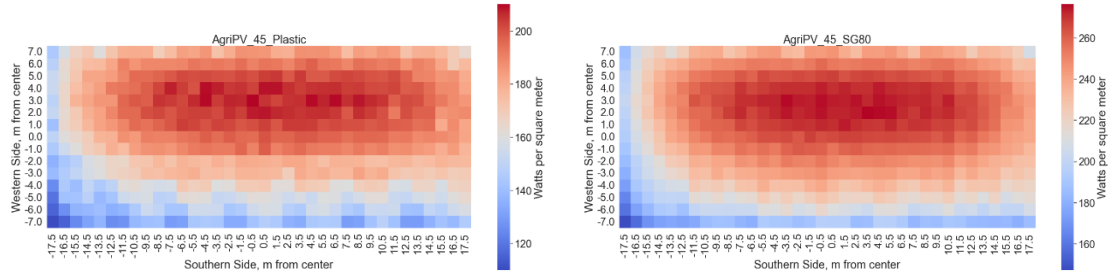

(a) (b)

Figure 13. Heatmaps of ground irradiance with modules at a 45°tilt: (a) plastic-based, (b) SG80-based

The effect of increasing the bPV module tilt angle to 45° on irradiance distribution was evaluated using heatmaps shown in Figure 13. The SG80 cover provided a higher average irradiance of 226.32 W/m² with improved uniformity,

while the white plastic cover reached 172.17 W/m². As shown in Figure 14, the SG80 configuration demonstrated enhanced light availability and more uniform irradiance at 226.05 W/m², compared to the white plastic cover, which averaged 170.80 W/m² and exhibited several shaded areas.

This improvement is in line with the findings of Reher *et al.* (2024), who demonstrated that reducing the Ground Coverage Ratio (GCR) from 0.6 to 0.2 significantly improved irradiance uniformity and crop productivity. Together, these results highlight that both cover characteristics and system design play a critical role in controlling spatial light distribution and overall performance.

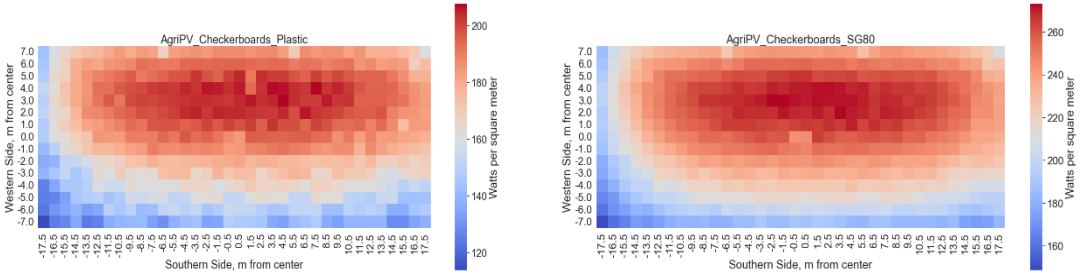

Figure 14. Heatmaps of ground irradiance with modules at a Checkerboard Pattern: (a) plastic-based, (b) SG80-based

3.3. Photosynthetically Active Radiation to LSP

This work evaluated ground-level irradiance under greenhouse and open-field setups using SG80 and plastic materials. The checkerboard SG80 configuration achieved the highest average irradiance, with 35° and 45° SG80 tilts following. Plastic-covered models performed lower, capturing only 74–80% of the irradiance observed in SG80 setups, as summarized in Figure 15. The standard SG80 configuration recorded an average irradiance of 252.62 W/m², equivalent to 1,151.95 µmol/m²/s, exceeding the LSP for tomato crops of 167.4 W/m². The plastic checkerboard model reached 170.80 W/m² and 778.85 µmol/m²/s, while the standard plastic model achieved 192.00 W/m² and 875.53 µmol/m²/s. Figure 16 illustrates that the SG80-based design provides higher light availability and better photosynthetic conditions, aligning with the findings of Prakash *et al.* (2023), where partial-density agrivoltaic systems achieved higher PAR values 282–1,135 µmol/m²/s and better light distribution than denser configurations.

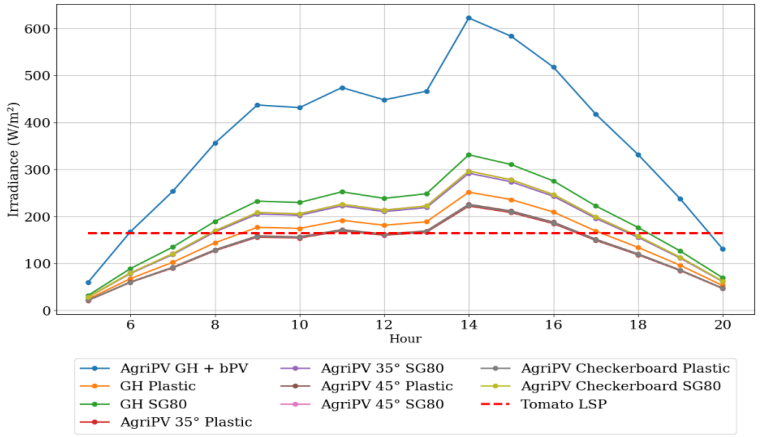

Figure 15. Comparison of average ground irradiance

The simulated irradiance results were further analyzed in relation to crop physiology, particularly the risk of photoinhibition, which occurs when light intensity exceeds the crop's LSP. In several configurations, such as the plastic checkerboard and SG80 setups, ground irradiance values slightly exceeded the tomato LSP threshold of 164.7 W/m². Nevertheless, these values remained within a tolerable range, indicating that although short-term peaks may

induce partial photoinhibition, the overall light distribution still supports efficient photosynthesis without significantly reducing crop productivity (Kitao *et al*., 2022). This finding underscores the importance of integrating ray tracing not only to optimize PV energy yield but also to evaluate agronomic light conditions, thereby ensuring that agrivoltaic systems achieve both energy efficiency and sustainable crop growth.

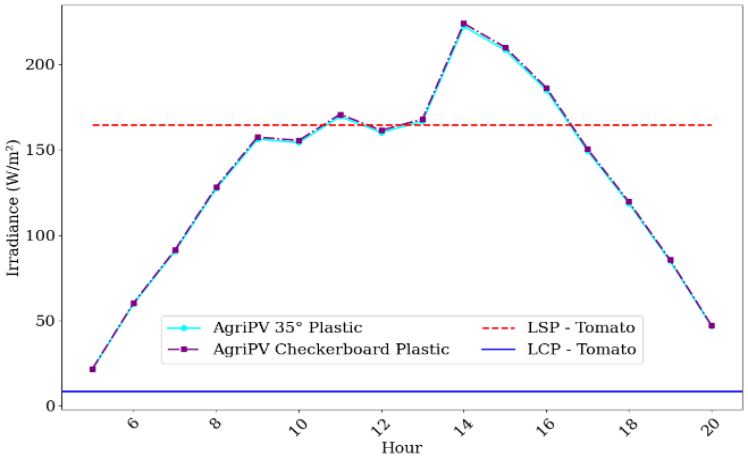

Figure 16. Daily irradiation profiles of the two optimal configurations

3.4. Energy Yield and Performance Analysis

The monthly energy analysis showed that both the 35° plastic-tilt and checkerboard configurations maintained ground-level irradiance near the tomato LSP 167.4 W/m², producing 50–60 kWh during low-sun months and peaking at about 150 kWh between June and August. As presented in Figure 17, the checkerboard setup outperformed the 35° tilt by up to 5% from May to September, mainly due to a rear-side irradiance contribution of 25–30% of the total irradiance. These results, obtained using bifacial modules with 20.38% efficiency and 0.7 bifaciality, are consistent with Prakash *et al*. (2023), validated PAR distribution under different panel densities using both field measurements and simulation models, finding strong agreement correlation coefficient (R = 0.99) but with slight overestimation 3.7–13.5%. Beyond this validation, the present study extends existing knowledge by linking irradiance distribution to seasonal energy yield and rear-side bifacial performance, thereby highlighting the checkerboard configuration as a practical design solution that optimizes both energy generation and crop-level light conditions compared with density-based approaches.

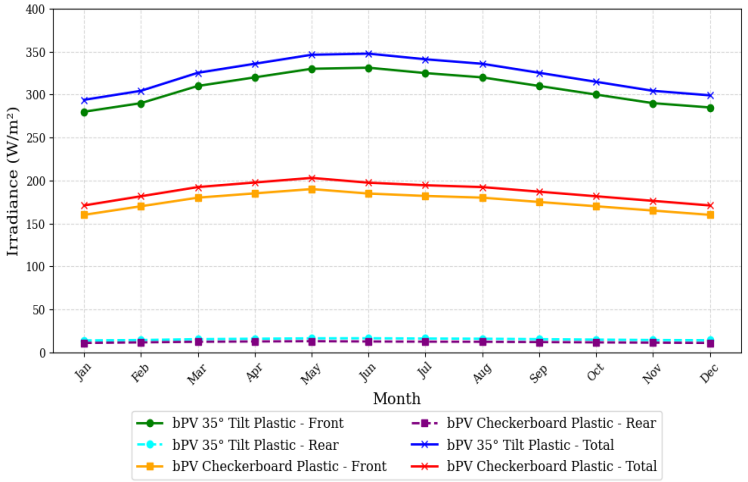

Figure 17. Graph of monthly energy yield

4. CONCLUSION

This work established a simulation framework that combined ray tracing-based optical modeling with irradiance and energy analysis to evaluate the integration of bPV systems in agrivoltaic greenhouses. Among all tested configurations, only the 35° plastic tilt and plastic checkerboard models achieved ground-level irradiance values close to the LSP threshold of 167.4 W/m², maintaining compatibility with crop photosynthetic requirements while producing seasonal energy yields ranging from 50.0 to 150.0 kWh. The plastic checkerboard model demonstrated superior rear-side irradiance utilization, contributing 25–30% of total irradiance and achieving a bifacial gain of 6.84%, compared to 4.946% in the 35° model. While the tilt configuration relied heavily on front-side irradiance and produced a slightly higher total energy yield, the checkerboard model provided more uniform light distribution beneath the canopy, supporting improved growth conditions for light-sensitive crops. Although some setups slightly exceeded the LSP, irradiance levels remained within acceptable limits, indicating only minor photoinhibition risks. Based on these findings, the plastic checkerboard configuration is recommended as the most balanced option for optimizing energy performance and agronomic viability. Future work should integrate dynamic environmental variables and develop real-time simulation tools to support broader adoption in precision-controlled greenhouse applications. This study, however, is based entirely on numerical simulations and does not include experimental validation. Therefore, the results should be interpreted as indicative rather than definitive.

AUTHOR CONTRIBUTION STATEMENT

Author	C	M	So	Va	Fo	I	R	D	O	E	Vi	Su	P	Fu
EW	✓	✓	✓	✓	✓	✓		✓	✓	✓	✓		✓	
Sub	✓		✓	✓				✓	✓	✓	✓	✓		✓
BS			✓					✓				✓		
SR										✓		✓	✓	
BS		✓					✓			✓		✓		
RAA	✓					✓		✓		✓		✓		
MNS		✓					✓			✓		✓		
AHA					✓		✓			✓		✓		
DS	✓		✓			✓			✓					
AF			✓			✓			✓					
AW			✓				✓		✓					
IGBJ									✓	✓			✓	

C: Conceptualization
M: Methodology
So: Software
Va: Validation
Fo: Formal Analysis
I: Investigation
D: Data Curation
R: Resources
O: Writing - Original Draft
E: Writing - Review & Editing
Vi: Visualization
Su: Supervision
Fu: Funding Acquisition
P: Project Administration

ACKNOWLEDGMENTS

This work was supported by UEESRG (UNNES Electrical Engineering Students Research Group), Department of Electrical Engineering, Universitas Negeri Semarang, in facilitating this study. Additionally, funding for this research was sponsored by Direktorat Riset, Teknologi, dan Pengabdian Masyarakat, Direktorat Jenderal Pendidikan Tinggi, Riset, dan Teknologi, Kementerian Pendidikan, Kebudayaan, Riset, dan Teknologi, under grant no. 031/E5/PG.02.00/PL.BATCH.2/2024 with contract no. 5.2.8/UN37/PPK.10/2024.

REFERENCES

Angmo, P., Dolma, T., Phuntsog, N., Chaurasia, O.P., & Stobdan, T. (2022). Effect of shading and high temperature amplitude on yield and phenolic contents of greenhouse Capsicum (*Capsicum annuum* L.). *Open Access Research Journal of Biology and Pharmacy*, ***4***(1), 30–39. https://doi.org/10.53022/oarjbp.2022.4.1.0053

Ayala Pelaez, S. (2019). Bifacial solar panels system design, modeling, and performance. [*Doctoral dissertation*]. University of Arizona Campus Repository. http://hdl.handle.net/10150/631283

Ayala Pelaez, S., & Deline, C. (2020). Bifacial_radiance: A python package for modeling bifacial solar photovoltaic systems. *Journal of Open Source Software*, ***5***(50), 1865. https://doi.org/10.21105/joss.01865

Bantis, F., Chatzigeorgiou, I., Sismanis, M., Ntinas, G.K., & Koukounaras, A. (2024). Vegetable production in PFALs: Control of micro-environmental factors, principal components and automated systems. *Agriculture*, ***14***(4), 642. https://doi.org/10.3390/agriculture14040642

De Soto, W., Klein, S.A., & Beckman, W.A. (2006). Improvement and validation of a model for photovoltaic array performance. *Solar Energy*, ***80***(1), 78–88. https://doi.org/10.1016/j.solener.2005.06.010

Direktorat Sayuran dan Tanaman Obat, Direktorat Jenderal Hortikultura, Kementerian Pertanian. (2021). *Standar minimal greenhouse*. Kementerian Pertanian.

Ernst, M., Asselineau, C.-A., Tillmann, P., Jäger, K., & Becker, C. (2024a). Modelling bifacial irradiance – Step-by-step comparison and validation of view factor and ray tracing models. *Applied Energy*, ***369***, 123574. https://doi.org/10.1016/j.apenergy.2024.123574

Ernst, M., Conechado, G.E.J., & Asselineau, C.A. (2022). Accelerating the simulation of annual bifacial illumination of real photovoltaic systems with ray tracing. *IScience*, ***25***(1), 103698. https://doi.org/10.1016/j.isci.2021.103698

Ernst, M., Liu, X., Asselineau, C.-A., Chen, D., Huang, C., & Lennon, A. (2024b). Accurate modelling of the bifacial gain potential of rooftop solar photovoltaic systems. *Energy Conversion and Management*, ***300***, 117947. https://doi.org/10.1016/j.enconman.2023.117947

Fathabadi, H. (2015). Lambert W function-based technique for tracking the maximum power point of PV modules connected in various configurations. *Renewable Energy*, ***74***, 214–226. https://doi.org/10.1016/j.renene.2014.07.059

Grommes, E.-M., Schemann, F., Klag, F., Nows, S., & Blieske, U. (2023). Simulation of the irradiance and yield calculation of bifacial PV systems in the USA and Germany by combining ray tracing and view factor model. *EPJ Photovoltaics*, ***14***, 11. https://doi.org/10.1051/epjpv/2023003

Gu, W., Ma, T., Li, M., Shen, L., & Zhang, Y. (2020). A coupled optical-electrical-thermal model of the bifacial photovoltaic module. *Applied Energy*, ***258***, 114075. https://doi.org/10.1016/j.apenergy.2019.114075

Hansen, C.W., Stein, J.S., Deline, C., MacAlpine, S., Marion, B., Asgharzadeh, A., & Toor, F. (2016). Analysis of irradiance models for bifacial PV modules. *2016 IEEE 43rd Photovoltaic Specialists Conference (PVSC)*, 0138–0143. https://doi.org/10.1109/PVSC.2016.7749564

International Electrotechnical Commission [IEC]. (2022). *IEC 60904: Photovoltaic devices—Part 1-2: Measurement of current–voltage characteristics of bifacial photovoltaic (PV) devices (Draft A)*. International Electrotechnical Commission.

International Electrotechnical Commission. (2022). *Photovoltaic devices – Part 1-2: Measurement of current-voltage characteristics of bifacial photovoltaic (PV) devices* (Draft A).

Katsikogiannis, O.A., Ziar, H., & Isabella, O. (2022). Integration of bifacial photovoltaics in agrivoltaic systems: A synergistic design approach. *Applied Energy*, ***309***, 118475. https://doi.org/10.1016/j.apenergy.2021.118475

Kitao, M., Yazaki, K., Tobita, H., Agathokleous, E., Kishimoto, J., Takabayashi, A., & Tanaka, R. (2022). Exposure to strong irradiance exacerbates photoinhibition and suppresses N resorption during leaf senescence in shade-grown seedlings of fullmoon maple (*Acer japonicum*). *Frontiers in Plant Science*, ***13***. https://doi.org/10.3389/fpls.2022.1006413

Kujawa, A., Hanrieder, N., Wilbert, S., Fernández Solas, Á., González Rodríguez, S., Alonso-García, M. del C., Polo, J., Carballo, J. A., López-Díaz, G., Cornaro, C., & Pitz-Paal, R. (2025). A ray-tracing-based irradiance model for agrivoltaic greenhouses: Development and application. *Agronomy*, ***15***(3), 665. https://doi.org/10.3390/agronomy15030665

Laue, T. (2022). Using Ray Tracing to Model Agri-PV Greenhouse Energy Production and PAR Levels. [*Master's thesis*]. University of Oslo, Oslo, Norway.

Leng, W., Wang, T., Wang, G., Letu, H., Wang, S., Xian, Y., Yan, X., & Zhang, Z. (2023). All-sky surface and top-of-atmosphere shortwave radiation components estimation: Surface shortwave radiation, PAR, UV radiation, and TOA albedo. *Remote Sensing of Environment*, ***298***, 113830. https://doi.org/10.1016/j.rse.2023.113830

Lewis, M.R., Coathup, T.J., Russell, A.C.J., Guerrero-Perez, J., Valdivia, C.E., & Hinzer, K. (2024). Quantifying structural shading and reflection effects on single axis tracked bifacial photovoltaic system performance. *Advanced Energy and Sustainability Research*, ***5***(8), 2400007. https://doi.org/10.1002/aesr.202400007

Mamun, M.A.Al., Dargusch, P., Wadley, D., Zulkarnain, N.A., & Aziz, A.A. (2022). A review of research on agrivoltaic systems. *Renewable and Sustainable Energy Reviews*, ***161***, 112351. https://doi.org/10.1016/j.rser.2022.112351

National Renewable Energy Laboratory. (2021). *EnergyPlus (Version 9.5) [Software]*. https://energyplus.net/weather/sources#IWEC

Pettersen, A. (2019). The performance of household PV systems in Southeastern Norway. [*Master's thesis*]. Norwegian University of Life Sciences.

Prakash, V., Lunagaria, M.M., Trivedi, A.P., Upadhyaya, A., Kumar, R., Das, A., Gupta, A.K., & Kumar, Y. (2023). Shading and PAR under different density agrivoltaic systems, their simulation and effect on wheat productivity. *European Journal of Agronomy*, ***149***, 126922. https://doi.org/10.1016/j.eja.2023.126922

Reher, T., Lavaert, C., Willockx, B., Huyghe, Y., Bisschop, J., Martens, J.A., Diels, J., Cappelle, J., & Van de Poel, B. (2024). Potential of sugar beet (*Beta vulgaris*) and wheat (*Triticum aestivum*) production in vertical bifacial, tracked, or elevated agrivoltaic systems in Belgium. *Applied Energy*, ***359***, 122679. https://doi.org/10.1016/j.apenergy.2024.122679

Rezaei, F., Burg, V., Pfister, S., Hellweg, S., & Roshandel, R. (2024). Optimization framework of clean heat and CO_2 supply for agricultural greenhouses exploiting industrial symbiosis. *Energy Strategy Reviews*, ***55***, 101509. https://doi.org/10.1016/j.esr.2024.101509

Robsahm, A.E. (2023). Simulation of a vertical bifacial PV system compared to measured values. [*Master's thesis*]. Norwegian University of Life Sciences.

Russell, A.C.J., Valdivia, C.E., Bohemier, C., Haysom, J.E., & Hinzer, K. (2022). DUET: A novel energy yield model with 3-d shading for bifacial photovoltaic systems. *IEEE Journal of Photovoltaics*, ***12***(6), 1576–1585. https://doi.org/10.1109/JPHOTOV.2022.3185546

Solcast. (2021). *Solcast – Solar forecasting & solar irradiance data*. Retrieved from https://solcast.com/

Teitel, M., Grimberg, R., Ozer, S., Vitoshkin, H., Yehia, I., Magadley, E., Levi, A., Ziffer, E., Gantz, S., & Levy, A. (2023). Effects of organic photovoltaic modules installed inside greenhouses on microclimate and plants. *Biosystems Engineering*, ***232***, 81–96. https://doi.org/10.1016/j.biosystemseng.2023.06.012

Tripathy, M., Kumar, M., & Sadhu, P. K. (2017). Photovoltaic system using Lambert W function-based technique. *Solar Energy*, ***158***, 432–439. https://doi.org/10.1016/j.solener.2017.10.007

Xiong, W., Deng, X., Liu, Z., Liu, R., Wu, Z., & Zhang, L. (2022). Sustainability and efficient use of building-integrated photovoltaic curtain wall array (BI-PVCWA) systems in building complex scenarios. *Energy and Buildings*, ***276***, 112477. https://doi.org/10.1016/j.enbuild.2022.112477

Zhang, Q., Peng, J., Luo, Y., Wang, M., Wang, S., Tan, Y., & Ma, T. (2025a). Development of a novel power generation model for bifacial photovoltaic modules based on dynamic bifaciality. *Energy Conversion and Management*, ***324***, 119305. https://doi.org/10.1016/j.enconman.2024.119305

Zhang, W., Yue, Z., Ma, H., Gao, Y., Liu, W., Huang, X., Zhang, L., Meng, X., Kribus, A., Vitoshkin, H., Liu, W., & Zhang, X. (2024). Agricultural friendly single-axis dynamic agrivoltaics: Simulations, experiments and a large-scale application for Chinese solar greenhouses. *Applied Energy*, ***374***, 123891. https://doi.org/10.1016/j.apenergy.2024.123891

Zhang, X., Yang, K., Shao, C., & Chen, H. (2025b). A novel parameterization scheme for accurate and efficient radiation transfer modeling in large-scale PV power plants. *Applied Energy*, ***384***, 125423. https://doi.org/10.1016/j.apenergy.2025.125423

Zhu, L., Li, Q., Chen, M., Cao, K., & Sun, Y. (2019). A simplified mathematical model for power output predicting of Building Integrated Photovoltaic under partial shading conditions. *Energy Conversion and Management*, ***180***, 831–843. https://doi.org/10.1016/j.enconman.2018.11.036

Zohdi, T.I. (2021). A digital-twin and machine-learning framework for the design of multiobjective agrophotovoltaic solar farms. *Computational Mechanics*, ***68***(2), 357–370. https://doi.org/10.1007/s00466-021-02035-z